Applied Surface Science 579 (2022) 152234

Contents lists available at ScienceDirect

Applied Surface Science

journal homepage: www.elsevier.com/locate/apsusc

Full Length Article

Non-precious metal activated $MoSi_2N_4$ monolayers for high-performance OER and ORR electrocatalysts: A first-principles study

Song Lu [a], Yang Zhang [a,b], Fengliu Lou [b], Kun Guo [c,*], Zhixin Yu [a,*]

[a] Department of Energy and Petroleum Engineering, University of Stavanger, 4036 Stavanger, Norway
[b] Beyonder AS, Kanalsletta 2, 4033 Stavanger, Norway
[c] Institute of New Energy, School of Chemistry and Chemical Engineering, Shaoxing University, Shaoxing 312000, China

ARTICLE INFO

Keywords:
$MoSi_2N_4$
$TM-N_4$ moiety
Single atom catalysts
OER/ORR overpotential
Dual-site mechanism

ABSTRACT

Developing high-performance electrocatalysts for oxygen evolution reaction (OER) and oxygen reduction reaction (ORR) is crucial for energy conversion and storage. Recently, a new type of two-dimensional material $MoSi_2N_4$ was successfully synthesized and received considerable attention because of novel properties and potential applications. Herein, by means of first principles calculation, the OER/ORR activities of 3*d* transition metal (TM) atoms embedded $MoSi_2N_4$ (TM@MSN) were investigated. The calculated results indicate that TM atoms on $MoSi_2N_4$ exhibit good electrochemical stability. On TM sites, Ti@MSN shows the highest OER activity with an overpotential of 0.48 V, whereas Cr@MSN is the most active ORR catalyst with an overpotential of 0.48 V. The Si site (Si−N1−Cu) of Cu@MSN follows the dual-site mechanism, exhibiting the same OER/ORR overpotential as that of N site (0.55/0.65 V). Interestingly, the outer N site (Zn−N1) of Zn@MSN achieves the lowest OER overpotential of 0.38 V, better than that of the state-of-the-art RuO_2 catalyst. We demonstrate that 3*d* TM atoms not only serve as active sites themselves but also activate the host atoms to improve OER/ORR performance of $MoSi_2N_4$. Our work opens new windows of opportunity for developing novel catalysts beyond the precious metal-based electrocatalysts for efficient energy conversion and storage.

1. Introduction

The development of reliable and sustainable energy sources is urgently demanded due to the increasing consumption of fossil fuels and continuous deterioration of global environment. Even though substantial research efforts have been made in energy conversion and storage, such as fuel cells, water splitting and metal-air batteries, the efficiency of these technologies is still low for large-scale applications [1–4]. Two major processes, i.e., oxygen evolution reaction (OER) and oxygen reduction reaction (ORR), are the core of many electrochemical technologies [5]. However, both reactions suffer from sluggish reaction kinetics, which severely limits the energy conversion efficiency. To date, the most advanced electrocatalysts used in OER and ORR are noble metal-based materials. For instance, ruthenium and iridium oxides are OER benchmark electrocatalysts in water splitting, while Pt-based catalysts prevail in the ORR of fuel cells and air-metal batteries [6,7]. Nevertheless, issues in terms of their high price, limited reserve and poor stability drive the scientists to seek replacements. Noteworthily, the recent research on non-precious transition metal embedded two-dimensional (2D) materials provides a new route to develop high performance OER and ORR electrocatalysts [8–12].

2D material-based catalysts have been receiving intensive attractions in the past few years due to the distinct physiochemical properties such as high specific surface area [13–15]. Since the single layer graphene has been reported, many other 2D materials have been widely studied as potential catalysts for energy conversion and storage in both experimental and theoretical work [16–21]. For example, carbon-based 2D materials doped with transition metal (TM) exhibit excellent electrocatalytic activity towards OER and ORR due to improved conductivity and electron transfer between active sites and intermediates [22,23]. On the other hand, it has been disclosed that downscaling the catalysts could enhance the atom utilization and catalytic activity. Single atom catalysts (SACs) with 100% atom utilization have thus become exciting materials in the field of energy conversion and storage [24]. For instance, Fei et al. systemically studied the atomic structure and OER activity of Fe, Co and Ni SACs embedded in N-doped graphene, which demonstrated remarkable electrocatalytic activity with the active TM − N_4 centre [25]. They reported that only C and TM atoms can act as

* Corresponding authors.
E-mail addresses: kun.guo@usx.edu.cn (K. Guo), zhixin.yu@uis.no (Z. Yu).

https://doi.org/10.1016/j.apsusc.2021.152234
Received 19 August 2021; Received in revised form 11 December 2021; Accepted 14 December 2021
Available online 17 December 2021

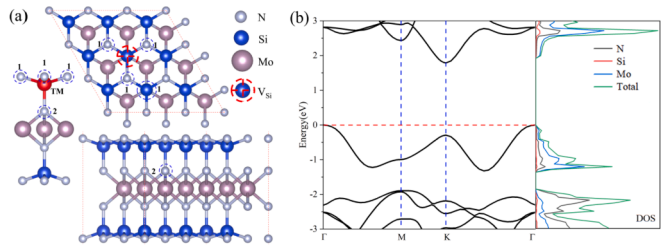

Fig. 1. (a) Top and side view of schematic structure of 3 × 3 × 1 $MoSi_2N_4$ monolayer with one Si vacancy the coordination, and the coordination environment of TM atom anchored on $MoSi_2N_4$; (b) Band structure and density of states (DOS) of each atom of $MoSi_2N_4$, where the Fermi level is set to zero (dashed line).

adsorption sites of intermediates. For Fe and Co SAC, all intermediates interact strongly with TM atoms. However, the *O and *OH intermediates are favourably adsorbed on C atoms for Ni SAC, while *OOH prefers to adsorb on Ni atom. Nonetheless, it is not always easy to attain SACs in terms of introducing two heteroatoms (N and TM atoms) to precisely build TM − N_4 active centres. Meanwhile, the activity is only demonstrated for some TM atoms, which limits the metal choices. Other 2D materials such as boron phosphide (BP) and graphitic carbon nitride (g-C_3N_4) have also been investigated as OER and ORR electrocatalysts [26,27]. Zeng et al. investigated that doping TM − N_3 moiety into BP exhibited excellent OER and ORR activity by first-principle calculations. They suggested that the OER/ORR performance of the TM site highly correlates with the electronic structures of its local environment [26]. Zheng et al. synthesized single Co atom embedded g-C_3N_4, which exhibited comparable OER and ORR activity to noble-metal catalysts [28]. A combination of experimental study and theoretical simulation revealed that the high activity originates from Co − N_2 moiety. In general, TM atoms rather than their coordinated non-metal atoms account for the activity of the SACs in OER and ORR. Therefore, activating host atoms of 2D materials by anchoring TM atoms will be of particular significance for designing high performance electrocatalysts.

Very recently, a new 2D material $MoSi_2N_4$ has been successfully fabricated by chemical vapor deposition and exhibits intriguing electrical and mechanical properties [29]. For instance, it has been demonstrated that the 2D $MoSi_2N_4$ is applicable in spintronic devices [30]. Bafekry et al. studied the effects of vacancy defects, atom adsorption and atom doping on the electronic and magnetic properties of $MoSi_2N_4$ via density functional theory (DFT) [31]. They disclosed that all defects narrow the bandgap of $MoSi_2N_4$ monolayer, and $MoSi_2N_4$ with a Si vacancy exhibits half-metallic attribute. Wu et al. reported that strain could induce its transition from indirect bandgap to direct bandgap, and the electric field can induce a transition from semiconductor to metal [32]. Mortazavi et al. suggested that $MoSi_2N_4$ nanosheet is a promising photocatalysts for water splitting [33]. It is known that defects commonly exist in 2D materials and modify the catalytic properties [34]. Zang et al. conducted a systematic investigation on the hydrogen evolution reaction (HER) over 2D $MoSi_2N_4$ by first-principle calculations [35]. They uncovered that the comparable high HER performance of $MoSi_2N_4$ to that of Pt catalysts is triggered by N vacancy defects. Meanwhile, they also found that doping TM atom further enhances the HER activity of $MoSi_2N_4$. Moreover, there is a novel structure in $MoSi_2N_4$ in which one Si atom is coordinated with four N atoms to form special Si − N_4. It is expected that embedding single TM atom into the Si vacancy of $MoSi_2N_4$ to construct TM − N_4 moiety is a promising approach to design advanced OER and ORR electrocatalysts for energy conversion and storage. To the best of our knowledge, there is little study on 2D $MoSi_2N_4$ or TM modified 2D $MoSi_2N_4$ for electrocatalytic OER and ORR reactions.

In this work, we embedded a series of 3*d* TM atoms (Sc, Ti, V, Cr, Mn, Fe, Co, Ni, Cu and Zn) into defective $MoSi_2N_4$ monolayer (TM@MSN) to build special TM − N_4 moiety to investigate their OER and ORR activity via first-principles calculations. The calculated results suggest that TM atoms could substantially enhance the OER and ORR performance of $MoSi_2N_4$ by activating the TM coordinated N atoms. Namely, TM atoms are not the sole active sites, whereas the coordinated N atoms could also act as catalytically active sites.

2. Computational method

A 3 × 3 × 1 supercell ($Mo_9Si_{18}N_{36}$) with 63 atoms was built (Fig. 1a). The 3*d* TM atom was embedded into Si vacancy created by removing one Si atom from the supercell. All first-principles calculations based on spin-polarized DFT were conducted in the Vienna Ab-initio Simulation Package (VASP) software [36,37]. The electron exchange–correlation interactions were described by the Perdew-Burke-Ernzerhof (PBE) functional within the generalized gradient approximation (GGA) [38–40]. The DFT-D3 semiempirical method proposed by Grimme was used to correct the long-range van der Waals interaction [41]. The parameter for dipole correction was also included in our calculations. The GGA + U correction was included for the *d*-electrons of TM atoms. A large vacuum space in the *z*-direction with more than 20 Å is enough to avoid spurious interactions between adjacent images. A cut-off energy of 500 eV was chosen for plane wave basis set. The convergence criterion for energy and force was set to 1.0 × 10^{-5} eV and 1.0 × 10^{-2} eV/Å, respectively. A 5 × 5 × 1 k-point sampling was used for geometric optimization, while a more precise k-point of 9 × 9 × 1 was set to calculate electronic properties. To evaluate the stability of defective structure, the ab initio molecular dynamics (AIMD) simulation was conducted in an NVT ensemble under 300 K for 10 ps with a time step of 2 fs [42,43]. The implicit solvation model was considered by using VASPsol [44]. The kinetic study was conducted by the climbing image nudged elastic band method (CINEB) [45]. Charge transfer between TM atoms and MSN or TM@MSN and intermediates were analysed by Bader charge analysis. The crystal orbital Hamilton population (COHP) method was used to analyze interaction strength between catalysts and intermediates based on the LOBSTER package [46].

The formation energy of Si vacancy in MSN is calculated using Equation (1) below:

$$E_f(V_{Si}) = E(MSN - V_{Si}) + \mu(Si) - E(MSN) \quad (1)$$

where E(MSN-V_{Si}) and E(MSN) denote the total energy of defective and perfect MSN monolayer, respectively. μ(Si) represents the chemical potential of Si atom, and the reference phase is the bulk Si.

The binding energy E_b of TM atoms on defective MSN is obtained by Equation (2):

$$E_b = E(TM - MSN) - E(MSN - V_{Si}) - E(TM) \quad (2)$$

where E(TM-MSN), E(MSN-V_{Si}), E(TM) are the total energy of TM embedded MSN, defective MSN and single TM atom in vacuum. A more negative value of E_b indicates better thermodynamic stability.

The cohesive energy E_c of TM atom is defined by Equation (3):

$$E_c = E(TM - bulk)/n - E(TM) \quad (3)$$

where E(TM-bulk) and E(TM) indicate the energy of TM atom in their referenced bulk metal and single TM atom in vacuum, respectively. n is the number of TM atom in their reference phase.

The dissolution ability of TM atoms on defective MSN, represented by U_{diss}, is calculated by Equation (4) below [47,48]:

$$U_{diss} = U_{diss-bulk} - (E_b - E_c)/ne \quad (4)$$

where the $U_{diss\text{-}bulk}$ and n denote the standard dissolution potential of TM metal and the number of electron transfer in the dissolution process [49]. The negative E_b − E_c and positive U_{diss} indicate the thermodynamical and electrochemical stability of TM@MSN.

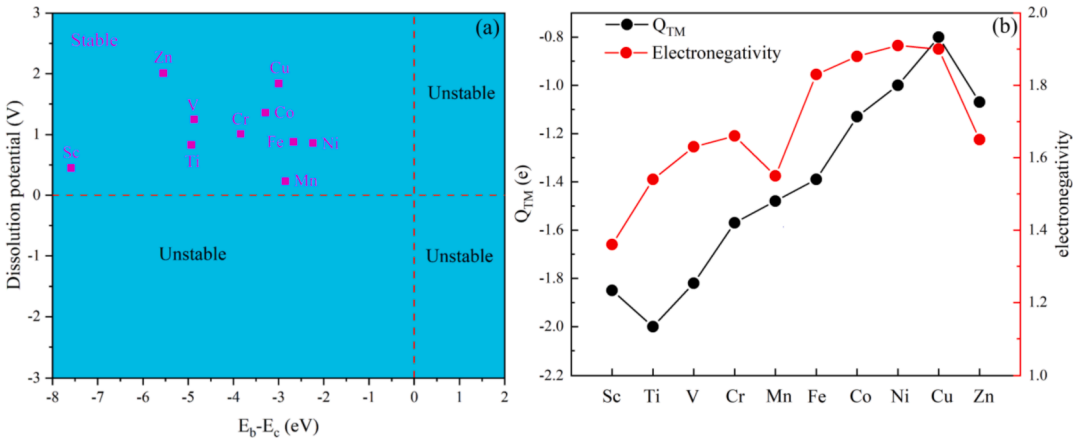

Fig. 2. (a) The dissolution potential (U_{diss}) of TM atoms against the binding energy and cohesive energy difference, where $E_b - E_c < 0$ and $U_{diss} > 0$ should be both satisfied for stable TM@MSN catalyst; (b) Charge transfer Q_{TM} (black line) and electronegativities (red line) of the TM atoms. (For interpretation of the references to colour in this figure legend, the reader is referred to the web version of this article.)

The elementary step of OER and ORR have been summarized below. In acidic medium (pH = 0), OER will occur through four elementary steps as Equations (5a)–(d):

$$H_2O\ (l) + *\rightarrow *OH + (H^+ + e^-) \quad (5a)$$

$$*OH \rightarrow *O + (H^+ + e^-) \quad (5b)$$

$$*O + H_2O\ (l) \rightarrow *OOH + (H^+ + e^-) \quad (5c)$$

$$*OOH \rightarrow O_2\ (g) + * + (H^+ + e^-) \quad (5d)$$

where * denotes the active site of electrocatalysts. In this work, three sites including TM, N1(TM − N1) and Si (Si − TM − N1) site are considered, where N1 is the three outer N atoms in Fig. 1a. *l* and *g* indicate the liquid and the gas phases, respectively. Based on an experimental reaction energy of 4.92 eV ($2H_2O \rightarrow O_2 + 2H_2$), the free energy of O_2 is obtained.

As ORR can be regarded as the reverse of OER, the elementary steps are expressed as Equations (6a)–(d):

$$O_2\ (g) + * + (H^+ + e^-) \rightarrow *OOH \quad (6a)$$

$$*OOH + (H^+ + e^-) \rightarrow *O + H_2O\ (l) \quad (6b)$$

$$*O + (H^+ + e^-) \rightarrow *OH \quad (6c)$$

$$*OH + (H^+ + e^-) \rightarrow H_2O\ (l) + * \quad (6d)$$

Under alkaline conditions, the four elementary steps for OER can be expressed as Equations (7a)–(d) below:

$$OH^- + * \rightarrow *OH + e^- \quad (7a)$$

$$*OH + OH^- \rightarrow *O + H_2O\ (l) + e^- \quad (7b)$$

$$*O + OH^- \rightarrow *OOH + e^- \quad (7c)$$

$$*OOH + OH^- \rightarrow O_2\ (g) + H_2O\ (l) + * + e^- \quad (7d)$$

The corresponding ORR steps can be written as Equations (8a)–(d) below:

$$O_2\ (g) + H_2O\ (l) + * + e^- \rightarrow *OOH + OH^- \quad (8a)$$

$$*OOH + e^- \rightarrow *O + OH^- \quad (8b)$$

$$*O + H_2O\ (l) + e^- \rightarrow *OH + OH^- \quad (8c)$$

$$*OH + e^- \rightarrow OH^- + * \quad (8d)$$

Based on the computational hydrogen electrode (CHE) model from Nørskov et al. [50], the Gibbs free energy change (ΔG) of each step in OER and ORR is calculated by Equation (9):

$$\Delta G = \Delta E + \Delta E_{ZPE} - T\Delta S + \Delta G_{pH} + \Delta G_U \quad (9)$$

where the ΔE, ΔE_{ZPE} and ΔS are the adsorption energy of intermediates, the change in zero-point energy and entropy contribution, respectively. The value of $\Delta E_{ZPE} - T\Delta S$ was fixed to be 0.35, 0.05 and 0.40 eV for *OH, *O and *OOH intermediates, respectively [50–52]. T is set to be 298.15 K. ΔG_{pH} is the free energy correction of proton concentration and is calculated by $\Delta G_{pH} = k_B T \ln 10 \times pH$. Although the ΔG of intermediates are related to ΔG_{pH}, the ΔG for each elementary reaction step is independent of pH. In this work, pH = 0 was chosen for acid environment. $\Delta G_{U=} -neU$, where n denotes the number of electrons and U is the electrode potential.

The free energy change in four elementary steps of OER is calculated as: $\Delta G_1 = G_{*OH}$, $\Delta G_2 = G_{*O} - G_{*OH}$, $\Delta G_3 = G_{*OOH} - G_{*O}$, $\Delta G_4 = 4.92 - G_{*OOH}$. Similarly, the Gibbs free energy change of ORR is obtained by: $\Delta G_a = G_{*OOH} - 4.92$, $\Delta G_b = G_{*O} - G_{*OOH}$, $\Delta G_c = G_{*OH} - G_{*O}$, $\Delta G_d = -G_{*OH}$.

The corresponding overpotentials are calculated as Equations (10a)–(b):

$$\eta(OER) = max\{\Delta G_1, \Delta G_2, \Delta G_3, \Delta G_4\}/e - 1.23 \quad (10a)$$

$$\eta(OER) = max\{\Delta G_a, \Delta G_b, \Delta G_c, \Delta G_d\}/e + 1.23 \quad (10b)$$

3. Results and discussion

3.1. Structure and stability of TM@MSN

After structure relaxation, the optimized lattice parameter *a* of pristine $MoSi_2N_4$ is 2.90 Å, which is in good agreement with previous studies [31,34,53]. As shown in Fig. 1a, three outer N atoms (N1) bond with one Si atom with the same bond length, indicating identical coordination environment. Meanwhile, an inner N atom (N2) bonds with a Mo atom, which has different chemical environment from the three outer N atoms. To build special TM − N_4 moiety, one Si atom was removed to form vacancy for TM atom anchoring. The formation energy of Si vacancy is 8.90 eV, slightly larger than that of defective graphene (7.69 eV) [54]. The stability of defective structure was evaluated by performing the AIMD simulation (Fig. S1). The total energy of defective MSN oscillates around the equilibrium state, accounting for the thermally stable defective structure. After anchoring the TM atoms, the lattice parameter *a* of TM@MSN barely changes (Table S1), which implies that the concentration of TM atom (1/63) is appropriate. The bond lengths of TM − N1 and TM − N2 exhibit appreciable elongation within

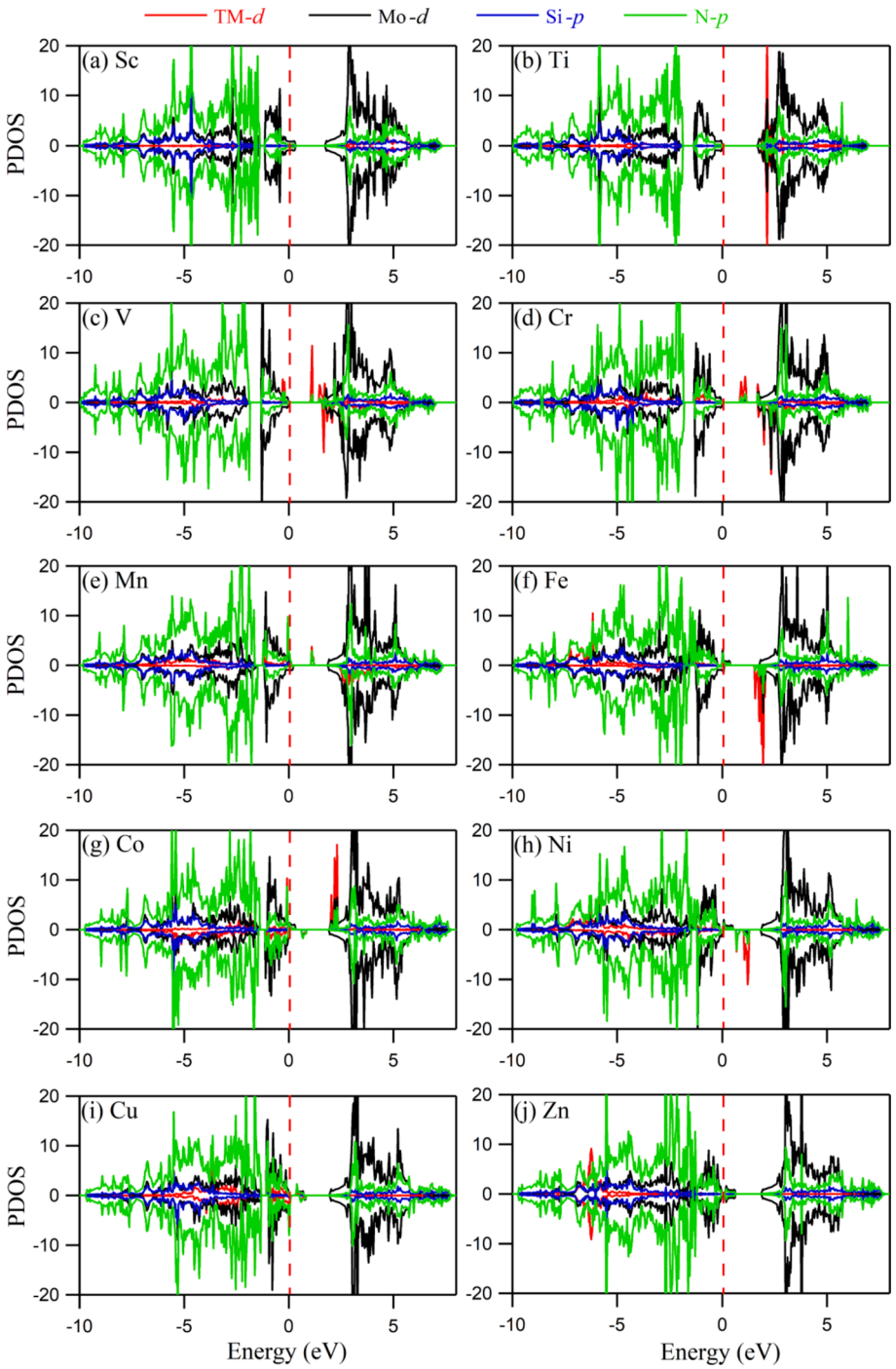

Fig. 3. The PDOS of TM@MSN, where the Fermi energy was set to zero (dashed line).

12.5% (N1) and 21.2% (N2) among all systems compared to Si − N1 or N2 of the pristine MSN due to the difference in atomic radius. The bond lengths of Si1-N1 were slightly influenced. Meanwhile, the bond lengths of TM − N1 and TM − N2 show a first decreasing and then increasing trend, in accordance with previous studies [55]. The changes are mainly caused by relaxing the newly formed TM-N1 bonds, which further affects the electronic structures of the surrounding atoms and modulates the catalytic performance.

The strong binding energy E_b between single TM atom and substrate could suppress the agglomeration of single atoms into clusters. The smaller the value of E_b, the tighter the TM atom is anchored into the defective structure. We considered the E_b of both Si vacancy and N vacancy (Table S1). Although the values of E_b on these two sites are all negative, TM atoms prefer to bind on Si vacancy due to the more negative binding energy. The calculated formation energy of N vacancy (N1) is 5.40 eV, smaller than the formation energy of Si vacancy at 8.90 eV. However, TM anchoring on Si vacancy site will be more stable and the stability of single TM atom affects the activity of SACs. Therefore, N vacancy site will not be further considered in this work. With the increase of the atomic number, E_b generally increases. Besides, we calculated the cohesive energy E_c to manifest the aggregation tendency of TM atoms on substrate. The differences $E_b - E_c$ are all negative in the range of − 2.24 to − 7.59 eV. We therefore anticipate that all SACs in this work can exhibit excellent structural stability. Moreover, the calculated dissolution potentials (U_{diss}) of all TM atoms on MSN are positive as shown in Fig. 2a and listed in Table S1, indicating good

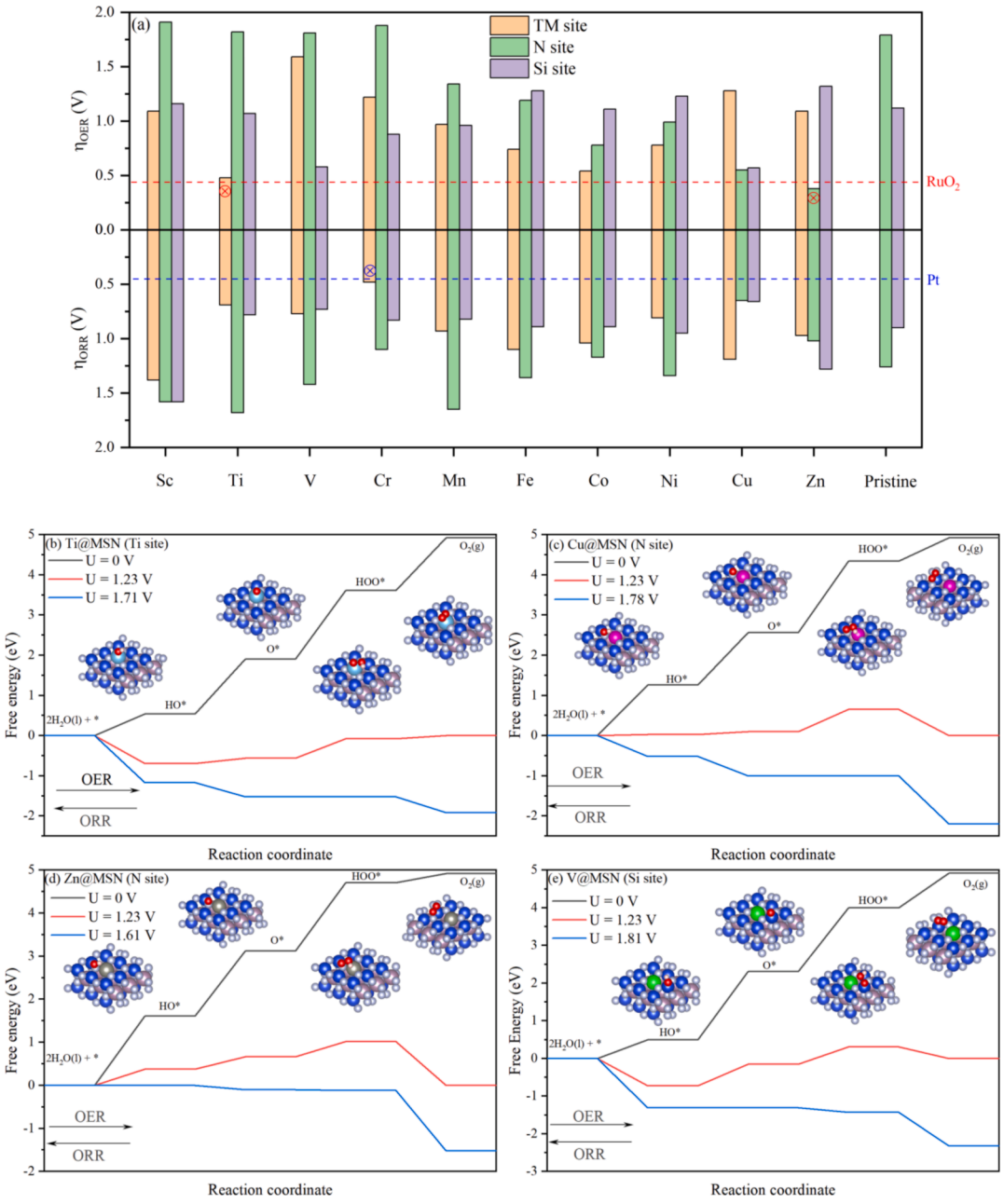

Fig. 4. (a) The OER and ORR overpotentials of TM@MSN on TM, N and Si sites, where the red and blue dash line represent the OER overpotential of RuO_2 and ORR overpotential of Pt, respectively; The OER and ORR Gibbs free energy diagrams of (b) Ti@MSN (Ti site), (c) Cu@MSN (N1 site), (d) Zn@MSN (N1 site), and (e) V@MSN (Si site). The black, red and blue lines denote different applied potentials; In the figures the optimized configuration of intermediates for each reaction step is shown. (For interpretation of the references to colour in this figure legend, the reader is referred to the web version of this article.)

electrochemical stability.

3.2. *Electronic structure of TM@MSN*

As depicted in Fig. 1b, the band structure of pristine $MoSi_2N_4$ reveals indirect bandgap of 1.77 eV between high symmetric points of Γ and K, consistent with previous studies in the same PBE level [34]. The total density of state (DOS) also suggests that the interactions between N and Si or Mo are of covalent nature. The valence band maximum (VBM) is mainly made up of N-*p* and Mo-*d* state, while the conduction band minimum (CBM) is contributed by Mo-*d* state. Besides, Bader charge analysis reveals charge transfer from the Si atoms (2.96e) to the proximate N atoms.

It has been well established that the electronic structures of host atoms can be effectively modulated by foreign atoms [56]. The charge density difference (CDD) (Fig. S2) shows electron transfer from the TM atoms to the bonding N atoms, while the Si atoms are basically not influenced by the embedded TM atoms. The CDD is calculated by $\Delta\rho = \rho(\text{TM@MSN}) - \rho(\text{MSN}) - \rho(\text{TM})$, where ρ(TM@MSN), ρ(MSN) and ρ(TM) are charge density of the TM anchored $MoSi_2N_4$, $MoSi_2N_4$ and TM atom, respectively. Meanwhile, electrons accumulate between the bond of TM − N, indicating the covalent bond nature. As shown in Table S1, all TM atoms on TM@MSN are positively charged as they act as electron donor. Thus, the positive charges on TM atom could effectively tune the position of *d*-band centres and improve the adsorption of intermediates during OER or ORR. Among which, Ti atom loses the largest amount of charges (2.00e), while Ni atom donates the least charges (1.00e). It is worth noting that the amount of charge loss of TM atoms is less than that

of host Si atoms, implying less charge was gained by N atoms when TM atom was embedded Si vacancy. This could affect the interaction strength between intermediates and N atoms, which may activate N as active sites for OER or ORR. Besides, we also find that the amount of charge transfer generally decreases with the increase of the atomic number, consistent with the overall change of electronegativity of 3*d*-TM atoms (Fig. 2b).

The magnetic property of TM@MSN was investigated by project density of state (PDOS), total density of state (DOS) and the results are presented in Fig. 3 and Fig. S3 and summarized in Table S1. The magnetic nature mainly originates from the 3*d* state of TM due to the asymmetric spin-up and spin-down channels. The magnetic moment increases and then decreases with the atomic number, consistent with other 3*d* TM atom modified systems [57]. Some localized states between the VBM and CBM can modify the electronic structure effectively. For instance, V, Cr, Mn, Fe, Co, Ni, Cu@MSN exhibit some impurity levels from TM-*d* state and N-*p* state, indicating decrease of the bandgap which can facilitate electron transfer. As a result, the electrical conductivity of these catalysts could be enhanced, further improving the electrocatalytic efficiency. Moreover, the PDOS of TM@MSN reveals a strong interaction between *p* orbitals of N atoms and *d* orbitals of TM atoms in conductive band or valence band. This suggests that TM atoms are the active sites for electrocatalytic reaction, resembling the reported TM $-$ N_4 moiety in other 2D materials.

3.3. OER and ORR performance of TM@MSN

To systematically investigate the OER and ORR performance over TM@MSN, the structures of *OH, *O and *OOH intermediates were fully optimized, and their corresponding Gibbs free energy change (ΔG) were calculated by Equation (10a) and b to obtain overpotentials. There are two types of sites (N1 and Si site) for intermediates adsorption for pristine MSN (Fig. 1a), while TM sites are considered as the adsorption sites for TM@MSN. Table S1 shows that the OER/ORR overpotentials on N and Si sites are 1.79/1.26 V and 1.12/0.90 V, respectively, suggesting that pristine MSN is not an active OER/ORR catalyst. The overpotential of TM@MSN for OER and ORR were calculated by Equations (8a) and (8b) (Fig. 4a). Noticeably, the embedded TM atoms lead to a major reduction of the OER/ORR overpotentials of MSN. The OER and ORR Gibbs free energy diagrams for each step on TM@MSN under U = 1.23 V were depicted in Fig. S4-S6. The OER reaction occurs from the left to right ($* + H_2O \rightarrow *OH \rightarrow *O \rightarrow *OOH \rightarrow O_2 + *$), while the ORR reaction is the reverse of OER. It is known that the ΔG of elementary steps on an ideal OER/ORR electrocatalyst is 1.23 eV with an overpotential of zero. However, the free energy difference of two neighbouring step is not always equal due to the different binding strengths between intermediates and active sites.

For TM site, it is found that OER and ORR are impeded at different stages due to the increase in Gibbs free energy. Meanwhile, TM@MSN mostly exhibits positive values of ΔG_{*OH}, ΔG_{*O} and ΔG_{*OOH} (Table S1), indicating weak interaction between active sites and intermediates. The potential determining steps (PDSs) of OER are identified as $* + H_2O \rightarrow *OH$ and $*O \rightarrow *OOH$, while the PDSs of ORR are $* + O_2 \rightarrow *OOH$ and $*OH \rightarrow * + H_2O$. Under U = 0 V, the ΔG for Ti@MSN in each OER step is 0.54, 1.36, 1.71, and 1.31 eV, respectively (Fig. 4b), yielding the smallest OER overpotential of 0.48 V. Cr@MSN presents the smallest ORR overpotential of 0.48 V, which is quite close to Pt at 0.45 V [58]. We then calculated the OER and ORR activity on N site. It can be found that the PDS of OER is the same as that on TM site. However, the PDSs of ORR are $* + O_2 \rightarrow *OOH$ and $*O \rightarrow *OH$. Fig. 4c shows that Cu@MSN has the lowest ORR overpotentials of 0.65 V on N site. Interestingly, N site in Zn@MSN presents the lowest OER overpotential of 0.38 V (Fig. 4d), which is even lower than the state-of-the-art RuO_2 electrocatalyst (0.42 V) [50]. For Si site, the PDSs of OER and ORR are $*OH \rightarrow *O$ and $* + O_2 \rightarrow *OOH$, respectively. The OER/ORR overpotentials of V@MSN are the lowest at 0.58/0.73 V (Fig. 4e), whereas other TM atoms slightly influence the OER/ORR overpotential on Si site. In addition, it turns out that the Si site of Cu@MSN has the same OER and ORR potentials (0.55/0.65 V) as the N site of Cu@MSN, which can be explained by the dual-site mechanism [25]. The *OH prefers to bind with Si atom, while the *O and *OOH are favorably adsorbed on the N atom (Fig. S7), resulting in low overpotential. Thus, embedded TM atom not only severs as active sites for OER and ORR, but also activates host atoms to boost the overall OER and ORR performance. In addition, as the TM atoms anchoring may affect the electronic structures of surrounding atoms such as N1, N2 and Si1, the binding strength between the intermediates and these atoms will be tuned. As shown in Fig. 4a, Si1 atom as the active centre can only slightly change the OER and ORR potential of pristine MSN. This is further confirmed by the lack of obvious changes in charge transfer of Si1 atom (Table S1 and Fig. S2). However, obvious change of charge transfer on N1 atom can be observed, indicating that the activity of N atom was greatly altered. This is evidenced by the change of OER and ORR overpotentials when N acts as the active center.

Solvent effect was considered by employing the implicit solvent model implemented in VASPsol with a dielectric constant of 78.4 for water. The ΔG of *OH, *O and *OOH on TM sites was calculated in Table S2 which shows an apparent increase of the overpotential of TM@MSN. It can be presumed that the implicit solvent model could generate more reliable results. Nevertheless, it has been demonstrated that OER and ORR studies without considering solvent effect could also give reasonable results [25,28]. Furthermore, the main purpose of our work is to screen $MoSi_2N_4$ based SACs from 3*d* group with the same criterion. Therefore, the solvent effect is not included in this work.

3.4. Reaction mechanisms

Generally, there are two possible mechanisms for ORR under acidic condition: associative and dissociative mechanism, which can be written as follows:

Associative: $O_2 + * \rightarrow *O_2$; $*O_2 + (H^+ + e^-) \rightarrow *OOH$; $*OOH + (H^+ + e^-) \rightarrow *O + H_2O$ or H_2O_2; $*O + (H^+ + e^-) \rightarrow *OH$; $*OH + (H^+ + e^-) \rightarrow H_2O + *$

Dissociative: $O_2 + * \rightarrow 2*O$;

$2*O + (H^+ + e^-) \rightarrow *O + *OH$; $O* + *OH + (H^+ + e^-) \rightarrow O* + H_2O$ or H_2O_2; $*O + (H^+ + e^-) \rightarrow *OH$; $*OH + (H^+ + e^-) \rightarrow H_2O + *$

The difference of the two mechanisms is whether the adsorbed O_2 molecule can be dissociated in the process. As shown the Fig. S8, the dissociation process on Cr@MSN need to overcome an energy barrier of 1.31 eV, which is larger than the associative barrier of 0.55 eV (Fig. S10). Thus, the associative mechanism is preferable.

The OER and ORRperformance of TM@MSN is further investigated by kinetic studies. Ti@MSN was calculated as an example for OER, while Cr@ORR was calculated for ORR. As shown in Fig. S9, the whole OER process on Ti@MSN is kinetically unfavourable. The third step to generate *OOH from *O and H_2O is the rate-limiting step with a large activation barrier of 1.59 eV. However, the ORR process on Cr@MSN is kinetically favourable (Fig. S10). The second protonation take places after O $-$ OH bond dissociation, forming *O and one H_2O molecule with a moderate activation barrier of 0.78 eV, which is regarded as the rate-limiting step in the ORR process.

On the other hand, there are different pathways to produce intermediates such as H_2O_2, *OH + *OH, *O + *OH in OER and ORR. The two-electron reduction process to generate H_2O_2 is the competing reaction to the four-electron reduction process. The two-electron process can be summarized as $O_2 + H^+ + e^- \rightarrow *OOH$ and $*OOH + H^+ + e^- \rightarrow H_2O_2$. Again using Cr@MSN as an example, for the two-electron reduction process, the ΔG for generating H_2O_2 during the second step of ORR is $-$ 0.21 eV (Fig. S11). On the other hand, the ΔG for *OH + *OH and *OH + *O are $-$ 0.09 and $-$ 0.37 eV, respectively. Despite that the ΔG for generating the three different intermediates are all negative, the ΔG from *OOH to *O is more negative at $-$ 2.45 eV. The energy barrier for the generation of H_2O_2 on Cr@MSN is 3.92 eV (Fig. S12),

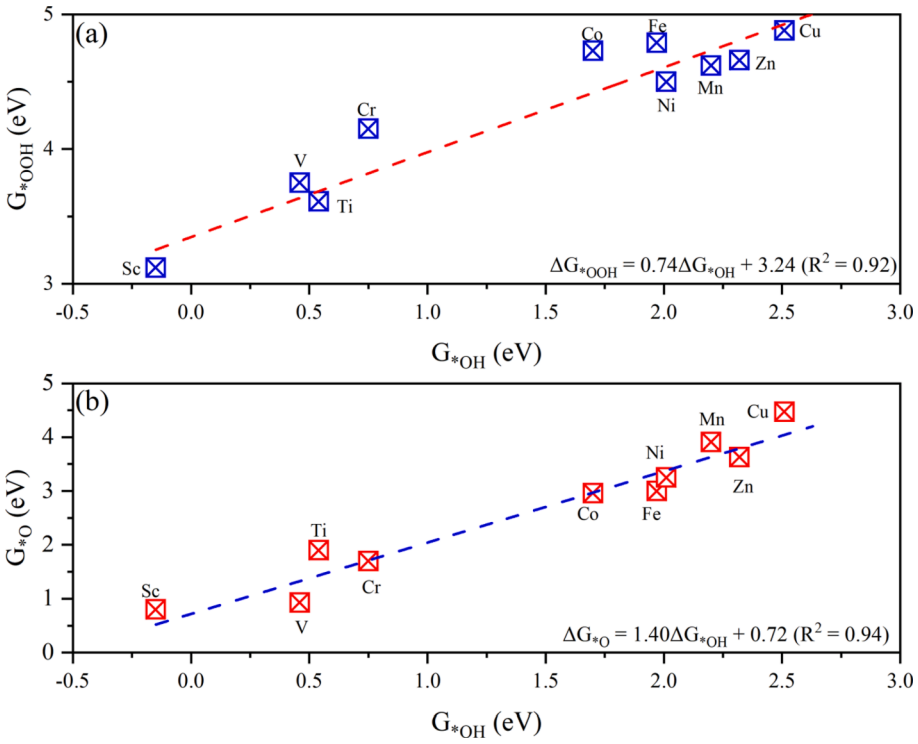

Fig. 5. Scaling relations between (a) ΔG_{*OH} and ΔG_{*OOH} and (b) ΔG_{*OH} and ΔG_{*O} for TM@MSN on TM site.

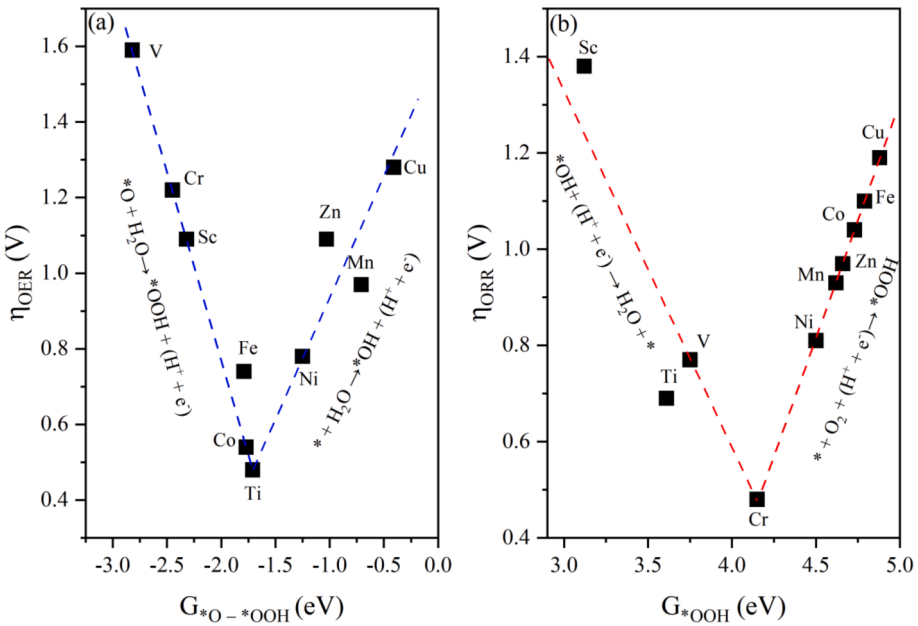

Fig. 6. The reverse volcano curve for TM@MSN on TM site; (a) OER overpotential (η_{OER}) and $\Delta G_{*O} - \Delta G_{*OOH}$, and (b) ORR overpotential (η_{ORR}) and ΔG_{*OOH}.

indicating that kinetic process is too harsh. Therefore, Cr@MSN has high selectivity for the pathway from *OOH to *O instead of from *OOH to *OH + *OH, *OH + *O or H_2O_2.

3.5. OER and ORR activity trends of TM@MSN

The Gibbs free energies of intermediates (ΔG_{*OH}, ΔG_{*O} and ΔG_{*OOH}) in OER/ORR processes have been regarded as useful descriptors for the interaction between intermediates and active sites, which can determine the overpotentials. Meanwhile, previous studies have disclosed that there exists a scaling relationship between the Gibbs free energy of *OH, *O and *OOH intermediates adsorbed on TM atoms. The scaling relationship between the Gibbs free energy of adsorbed intermediates was plotted in Fig. 5. The relationship between ΔG_{*OH} and ΔG_{*OOH} can be expressed as $\Delta G_{*OOH} = 0.74\Delta G_{*OH} + 3.24$, with a coefficient of determination (R^2) at 0.92 (Fig. 5a). The relationship between ΔG_{*OH} and ΔG_{*O} can be written as $\Delta G_{*O} = 1.40\Delta G_{*OH} + 0.72$, with R^2 at 0.94 (Fig. 5b). However, the relationships between these intermediates adsorbed on N and Si sites are not straight-forward. Thereafter, we will illustrate the activity trends only on the TM sites.

According to the well-established Sabatier principle [59], too strong or too weak interaction of adsorbates on TM@MSN could play negative

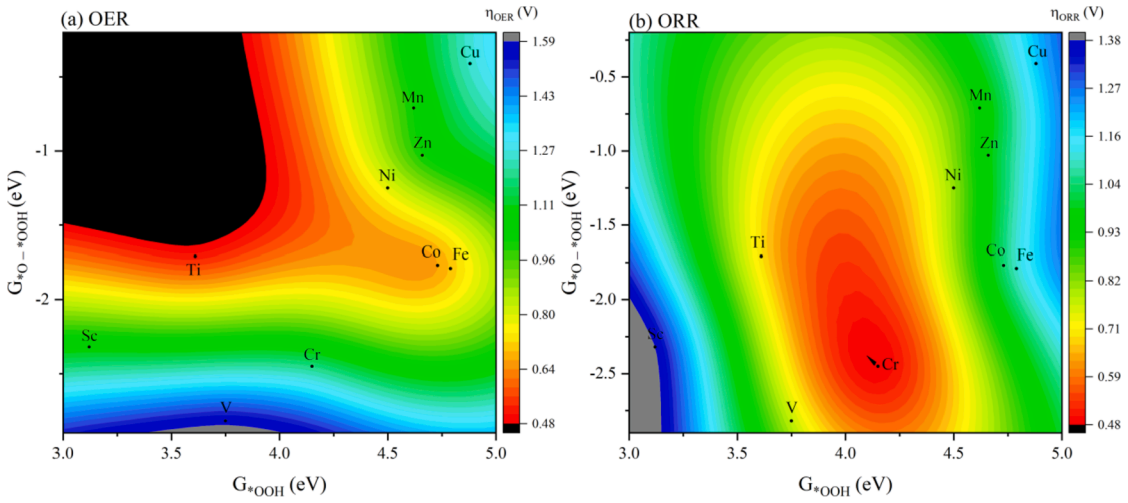

Fig. 7. The contour maps of (a) OER and (b) ORR activity trend over TM@MSN on TM site.

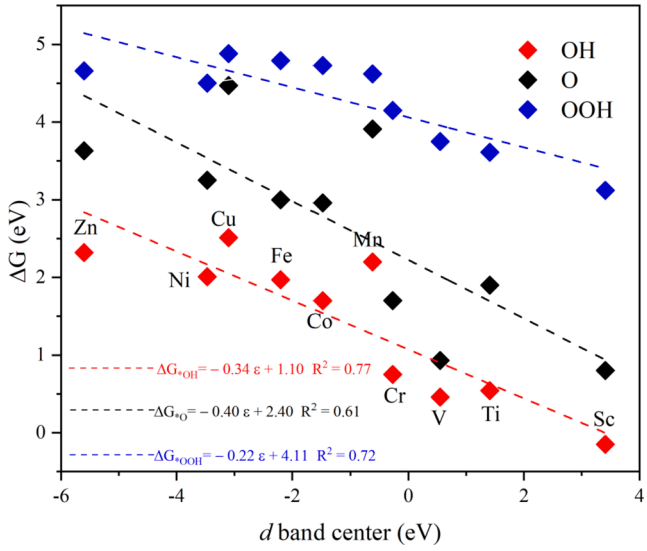

Fig. 8. The *d* band center (ε) against the Gibbs free energy of ΔG_{*OH}, ΔG_{*O} and ΔG_{*OOH} for TM@MSN on TM site.

roles on the catalytic performance. Too strong adsorption will inhibit the desorption of intermediates and poison the catalysts, while too weak interaction will not activate the reactants or intermediates for further reaction. For example, the interactions between the *OH, *O and *OOH intermediates on Sc@MSN and Cu@MSN electrocatalysts are relatively strong and weak, respectively. Thereby, their OER and ORR overpotentials are quite large. It can be seen from Fig. 6 that there are two reversed volcano plots by choosing $\Delta G_{*O} - \Delta G_{*OOH}$ and ΔG_{*OOH} as descriptors after being well fitted linearly, revealing the relationship between the Gibbs free energy of intermediates and overpotentials on TM sites in OER and ORR. The best catalysts with the moderate adsorption energy of intermediates shall sit on or near the top of the volcano. Accordingly, Ti@MSN with $\Delta G_{*O} - \Delta G_{*OOH}$ of − 1.71 eV is the best OER electrocatalysts, while the ΔG_{*OOH} is 4.15 eV for the best ORR electrocatalysts Cr@MSN. Nevertheless, we obtained the smallest OER overpotential based on $\Delta G_{*O} - \Delta G_{*OOH}$ of − 1.59 eV on N sites of Zn@MSN and a small ORR potential from ΔG_{*OOH} of 4.34 eV on N sites of Cu@MSN, demonstrating that the actual active sites are not limited to the TM atoms. Besides, three surface N1 atoms with identical chemical environment may serve as additional active sites for OER and ORR. Moreover, the contour maps of OER and ORR have been widely deployed to uncover the electrocatalytic activity trends [51,60]. The corresponding descriptors $\Delta G_{*O} - \Delta G_{*OOH}$ and ΔG_{*OOH} from the two reversed volcano can be combined to build contour maps. By employing these two descriptors, the contour maps of OER and ORR were constructed as in Fig. 7. It is again evident that the Ti@ and Cr@MSN occupy the highest activity regions and hence are the most promising OER and ORR catalysts.

3.6. The origin of OER and ORR activity of TM@MSN

The origin of OER and ORR activity on TM@MSN can be attributed to the variation of electronic structures. *d* band center (ε) is normally calculated to reveal the interaction strength between intermediates and electrocatalysts. As shown in Fig. 8 and Table S1, with the increase of the *d* electrons number of the TM atoms, the *d* band center generally shifts to more negative energy level with respect to Fermi level. It has been demonstrated that the larger number of *d* electrons of the TM atoms and lower energy level of the *d* band center will contribute to weaker interaction between substrates and intermediates. This can be explained by the *d* orbitals of TM atoms interacting with the electrons of intermediates as well as the charge transfer between intermediates and TM atoms [11]. Therefore, their hybridization could form bonding and antibonding states, directly affecting the adsorption free energy of intermediates [26]. Consequently, *d* band center can describe the ΔG and reveal the origin of catalytic activity. For instance, Sc@ and Zn@MSN show quite positive and negative *d* band center, which exhibit strong and weak interaction between intermediates and electrocatalysts, respectively. Therefore, both present large OER and ORR overpotential.

Furthermore, to gain insight of the excellent OER activity on Ti@MSN (TM site) and Zn@MSN (N site), the charge density difference and charge transfer on adsorbed intermediates were calculated. As illustrated in Fig. 9a and b, charge transfer and charge redistribution occurred between intermediates and the surface of Ti@MSN and Zn@MSN. For Ti as the bonding atom, the obtained net charges of intermediates are 0.51e, 0.94e and 0.57e for *OH, *O and *OOH, respectively. In contrast, the accepted net charges for *OH, *O and *OOH are 0.19e, 0.41e and 0.21e when N is the bonding atom on Zn@MSN. Remarkably, Ti atoms as the active center can donate more electrons to intermediates in comparison with N atom as the active center, implying that TM atoms could activate intermediates more effectively. By analyzing PDS, the key intermediate of OER on Ti@MSN and Zn@MSN can be assigned to be *O and *OH. We further studied the bonding and antibonding states of the absorbed key intermediates on the active atoms by employing COHP (Fig. 9c and d). It can be found that Ti@MSN shows obvious antibonding states near the Fermi level after the

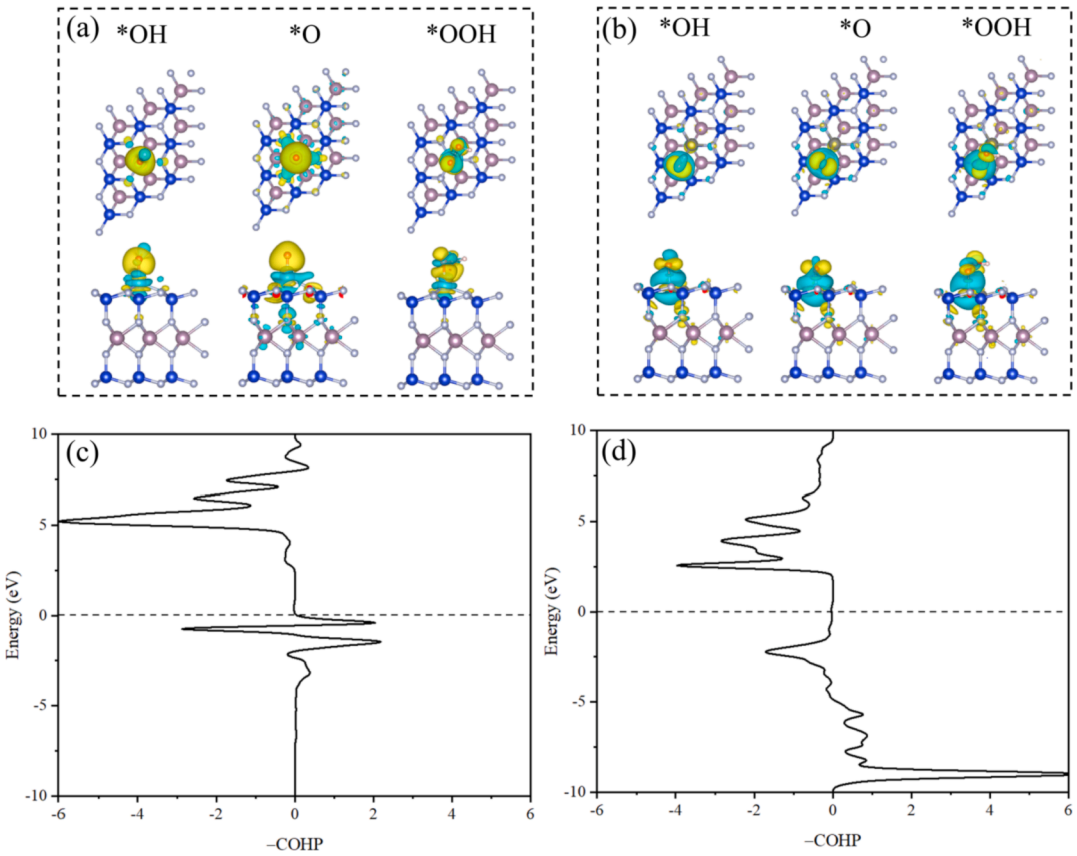

Fig. 9. The charge density difference of *OH, *O and *OOH intermediates adsorbed on (a) Ti@MSN (Ti site) and (b) Zn@MSN (N site), where yellow and cyan colors represent an increase and decrease in charge density, respectively. The COHP between Ti atom and *O on Ti@MSN (c) and between N atom and *OH on Zn@MSN (d). The isosurface value is set to be 0.003 e/Bohr^3. (For interpretation of the references to colour in this figure legend, the reader is referred to the web version of this article.)

adsorption of *O, indicating weak adsorption. Meanwhile, although small antibonding states appear on *OH adsorbed Zn@MSN, there are a lot of bonding states on Zn@MSN, suggesting strong adsorption. To give a more quantitative comparison, the integrated COHP (ICOHP) was calculated. Ti and Zn@MSN exhibit ICOHP of − 7.71 and − 8.03 eV, respectively. Therefore, *OH can be more stably adsorbed on the N atom, contributing to a small overpotential for the overall OER.

4. Conclusion

We systematically investigated the structure and stability and OER/ORR performance of 3*d* TM atoms embedded $MoSi_2N_4$ via first principles calculation. All TM atoms can be stably embedded into defective $MoSi_2N_4$ without agglomeration. Positive dissolution potentials of all TM atoms on $MoSi_2N_4$ indicates their good electrochemical stability. Mn, Fe, Co, Ni and Cu@MSN improves electrical conductivity of electrocatalysts, benefiting electron transfer during electrocatalytic reactions. For TM site, Ti@MSN shows the highest OER activity among all 3*d* TM atoms, with an overpotential of 0.48 V. Cr@MSN is the best ORR electrocatalyst among all catalysts. For N site, Zn@MSN has the lowest OER overpotential of 0.38 V, which is better than the state-of-the-art RuO_2 catalyst. Si and N sites of Cu@MSN exhibit the same OER and ORR overpotentials (0.55/0.65 V) because of the dual-site mechanism. On TM sites, the reversed volcano plots demonstrated that the OER overpotential is a function of $\Delta G_{*O} - \Delta G_{*OOH}$, while the ORR overpotential is a function of ΔG_{*OOH}. Two contour maps were constructed based on descriptors G_{*OOH}, $G_{*O} - G_{*OOH}$ and overpotential, which further disclosed the OER and ORR activity trends on TM@MSN. *d* band centre was used to clarify the origin of electrocatalytic activity attributed by moderate interaction strength between intermediates and catalysts. We also found that the anchored TM atoms not only sever as active sites but also activate the host atoms to improve the OER and ORR performance. Therefore, 3*d* TM atoms modified 2D $MoSi_2N_4$ can be an effective alternative to noble metal-based catalysts for energy conversion and storage.

CRediT authorship contribution statement

Song Lu: Methodology, Formal analysis, Investigation, Writing – original draft, Writing – review & editing, Visualization. **Yang Zhang:** Investigation, Formal analysis, Writing – review & editing. **Fengliu Lou:** Investigation, Formal analysis, Writing – review & editing. **Kun Guo:** Supervision, Writing – review & editing. **Zhixin Yu:** Conceptualization, Validation, Resources, Supervision, Writing – review & editing.

Declaration of Competing Interest

The authors declare that they have no known competing financial interests or personal relationships that could have appeared to influence the work reported in this paper.

Acknowledgement

This work was supported by the Norwegian Ministry of Education and Research. The computations were performed on resources provided by UNINETT Sigma2 – the National Infrastructure for High Performance Computing and Data Storage in Norway.

Appendix A. Supplementary material

Supplementary data to this article can be found online at https://doi.org/10.1016/j.apsusc.2021.152234.

References

[1] R. Cao, J.-S. Lee, M. Liu, J. Cho, Recent Progress in Non-Precious Catalysts for Metal- Air Batteries, Adv. Energy Mater. 2 (7) (2012) 816–829.
[2] Y. Li, H. Dai, Recent advances in zinc–air batteries, Chem. Soc. Rev. 43 (15) (2014) 5257–5275.
[3] M.I. Jamesh, X.M. Sun, Recent progress on earth abundant electrocatalysts for oxygen evolution reaction (OER) in alkaline medium to achieve efficient water splitting – A review, J. Power Sources 400 (2018) 31–68.
[4] L.J. Yang, J.L. Shui, L. Du, Y.Y. Shao, J. Liu, L.M. Dai, Z. Hu, Carbon-Based Metal-Free ORR Electrocatalysts for Fuel Cells: Past, Present, and Future, Adv. Mater. 31 (2019) 1804799.
[5] Z.W. Seh, J. Kibsgaard, C.F. Dickens, I.b. Chorkendorff, J.K. Nørskov, T. F. Jaramillo, Combining theory and experiment in electrocatalysis: Insights into materials design, Science 355, Science 355 (6321) (2017), https://doi.org/10.1126/science:aad4998.
[6] J. Rossmeisl, Z.-W. Qu, H. Zhu, G.-J. Kroes, J.K. Nørskov, Electrolysis of water on oxide surfaces, J. Electroanal. Chem. 607 (1-2) (2007) 83–89.
[7] A. Rabis, P. Rodriguez, T.J. Schmidt, Electrocatalysis for Polymer Electrolyte Fuel Cells: Recent Achievements and Future Challenges, ACS Catal. 2 (2012) 864–890.
[8] T.W. He, S.K. Matta, G. Will, A.J. Du, Transition-Metal Single Atoms Anchored on Graphdiyne as High-Efficiency Electrocatalysts for Water Splitting and Oxygen Reduction, Small Methods 3 (2019) 1800419.
[9] J. Deng, D.H. Deng, X.H. Bao, Robust Catalysis on 2D Materials Encapsulating Metals: Concept, Application, and Perspective, Adv. Mater. 29 (2017) 1606967.
[10] Y.N. Chen, X. Zhang, Z. Zhou, Carbon-Based Substrates for Highly Dispersed Nanoparticle and Even Single-Atom Electrocatalysts, Small Methods 3 (2019) 1900050.
[11] Y. Zhou, G. Gao, J. Kang, W. Chu, L.-W. Wang, Transition metal embedded two-dimensional C_3N as a highly active electrocatalyst for oxygen evolution and reduction reactions, J. Mater. Chem. A 7 (19) (2019) 12050–12059.
[12] T. Zhang, B. Zhang, Q. Peng, J. Zhou, Z. Sun, Mo_2B_2 MBene-supported single-atom catalysts as bifunctional HER/OER and OER/ORR electrocatalysts, J. Mater. Chem. A 9 (1) (2021) 433–441.
[13] X. Zhang, A. Chen, L.T. Chen, Z. Zhou, 2D Materials Bridging Experiments and Computations for Electro/Photocatalysis, Adv. Energy Mater. (2021) 2003841.
[14] X. Chia, M. Pumera, Characteristics and performance of two-dimensional materials for electrocatalysis, Nat Catal. 1 (12) (2018) 909–921.
[15] Z.H. Li, X. Zhang, H.F. Chen, J.W. Liu, M.F. Shao, M. Wei, D.G. Evans, H. Zhang, X. Duan, Confined Synthesis of 2D Nanostructured Materials toward Electrocatalysis, Adv. Energy Mater. 10 (2020) 1900486.
[16] J. Lim, J.-W. Jung, N.-Y. Kim, G.Y. Lee, H.J. Lee, Y. Lee, D.S. Choi, K.R. Yoon, Y.-H. Kim, I.-D. Kim, S.O. Kim, N_2-dopant of graphene with electrochemically switchable bifunctional ORR/OER catalysis for Zn-air battery, Energy Storage Mater. 32 (2020) 517–524.
[17] Y. Wu, C. Li, W. Liu, H. Li, Y. Gong, L. Niu, X. Liu, C. Sun, S. Xu, Unexpected monoatomic catalytic-host synergetic OER/ORR by graphitic carbon nitride: density functional theory, Nanoscale 11 (2019) 5064–5071.
[18] S. Back, S. Siahrostami, Noble metal supported hexagonal boron nitride for the oxygen reduction reaction: a DFT study, Nanoscale Adv. 1 (1) (2019) 132–139.
[19] Q. Wang, Y. Lei, Y. Wang, Y.i. Liu, C. Song, J. Zeng, Y. Song, X. Duan, D. Wang, Y. Li, Atomic-scale engineering of chemical-vapor-deposition-grown 2D transition metal dichalcogenides for electrocatalysis, Energy Environ. Sci. 13 (6) (2020) 1593–1616.
[20] A.S. Nair, R. Ahuja, B. Pathak, Unraveling the single-atom electrocatalytic activity of transition metal-doped phosphorene, Nanoscale Adv. 2 (6) (2020) 2410–2421.
[21] D. Kan, R. Lian, D. Wang, X. Zhang, J. Xu, X. Gao, Y. Yu, G. Chen, Y. Wei, Screening effective single-atom ORR and OER electrocatalysts from Pt decorated MXenes by first-principles calculations, J. Mater. Chem. A 8 (33) (2020) 17065–17077.
[22] X.-K. Kong, C.-L. Chen, Q.-W. Chen, Doped graphene for metal-free catalysis, Chem. Soc. Rev. 43 (8) (2014) 2841–2857.
[23] X.W. Wang, G.Z. Sun, P. Routh, D.H. Kim, W. Huang, P. Chen, Heteroatom-doped graphene materials: syntheses, properties and applications, Chem. Soc. Rev. 43 (2014) 7067–7098.
[24] B. Qiao, A. Wang, X. Yang, L.F. Allard, Z. Jiang, Y. Cui, J. Liu, J. Li, T. Zhang, Single-atom catalysis of CO oxidation using Pt_1/FeO_x, Nat. Chem. 3 (2011) 634.
[25] H. Fei, J. Dong, Y. Feng, C.S. Allen, C. Wan, B. Volosskiy, M. Li, Z. Zhao, Y. Wang, H. Sun, P. An, W. Chen, Z. Guo, C. Lee, D. Chen, I. Shakir, M. Liu, T. Hu, Y. Li, A. I. Kirkland, X. Duan, Y.u. Huang, General synthesis and definitive structural identification of MN4C4 single-atom catalysts with tunable electrocatalytic activities, Nat Catal. 1 (1) (2018) 63–72.
[26] H.H. Zeng, X.Y. Liu, F.B. Chen, Z.G. Chen, X.L. Fan, W.M. Lau, Single Atoms on a Nitrogen-Doped Boron Phosphide Monolayer: A New Promising Bifunctional Electrocatalyst for ORR and OER, ACS. Appl. Mater, Interfaces 12 (2020) 52549–52559.
[27] H. Niu, X. Wan, X. Wang, C. Shao, J. Robertson, Z. Zhang, Y. Guo, Single-Atom Rhodium on Defective g-C3N4: A Promising Bifunctional Oxygen Electrocatalyst, ACS Sustainable Chem. Eng. 9 (9) (2021) 3590–3599.
[28] Y. Zheng, Y. Jiao, Y. Zhu, Q. Cai, A. Vasileff, L.H. Li, Y.u. Han, Y. Chen, S.-Z. Qiao, Molecule-Level g-C3N4 Coordinated Transition Metals as a New Class of Electrocatalysts for Oxygen Electrode Reactions, J. Am. Chem. Soc. 139 (9) (2017) 3336–3339.
[29] Y.-L. Hong, Z. Liu, L. Wang, T. Zhou, W. Ma, C. Xu, S. Feng, L. Chen, M.-L. Chen, D.-M. Sun, X.-Q. Chen, H.-M. Cheng, W. Ren, Chemical vapor deposition of layered two-dimensional $MoSi_2N_4$ materials, Science 369 (6504) (2020) 670–674.
[30] Y. T. Bian, G. H. Liu, S. H. Qian, X. X. Ding, H. X. Liu, Effect of O-doping or N-vacancy on the structural, electronic and magnetic properties of $MoSi_2N_4$ monolayer, (2020) arXiv:2012.04162.
[31] A. Bafekry, M. Faraji, M.M. Fadlallah, A.B. Khatibani, A.A. Ziabari, M. Ghergherehchi, S. Nedaei, S.F. Shayesteh, D. Gogova, Tunable electronic and magnetic properties of $MoSi_2N_4$ monolayer via vacancy defects, atomic adsorption and atomic doping, Appl. Surf. Sci. 559 (2021), 149862.
[32] Q.Y. Wu, L.M. Cao, Y.S. Lin, L.K. Ang, Semiconductor-to-metal transition in bilayer MoSi2N4 and WSi2N4 with strain and electric field, Appl. Phys. Lett. 118 (2021), 113102.
[33] B. Mortazavi, B. Javvaji, F. Shojaei, T. Rabczuk, A.V. Shapeev, X. Zhuang, Exceptional piezoelectricity, high thermal conductivity and stiffness and promising photocatalysis in two-dimensional $MoSi_2N_4$ family confirmed by first-principles, Nano Energy 82 (2021), 105716.
[34] J. Zhu, S. Mu, Defect Engineering in Carbon-Based Electrocatalysts: Insight into Intrinsic Carbon Defects, Adv. Funct. Mater. 30 (25) (2020) 2001097, https://doi.org/10.1002/adfm.v30.2510.1002/adfm.202001097.
[35] Y.M. Zang, Q. Wu, W.H. Du, Y. Dai, B.B. Huang, Y.D. Ma, Activating electrocatalytic hydrogen evolution performance of two-dimensional MSi_2N_4 (M=Mo, W): A theoretical prediction, Phys. Rev. Materials 5 (2021), 045801.
[36] G. Kresse, D. Joubert, From ultrasoft pseudopotentials to the projector augmented-wave method, Phys. Rev. B 59 (1999) 1758.
[37] G. Kresse, J. Furthmüller, Efficiency of ab-initio total energy calculations for metals and semiconductors using a plane-wave basis set, Comput. Mater. Sci. 6 (1) (1996) 15–50.
[38] P.E. Blöchl, Projector augmented-wave method, Phys. Rev. B: Condens. Matter Mater. Phys. 50 (24) (1994) 17953–17979.
[39] J.P. Perdew, K. Burke, M. Ernzerhof, Generalized Gradient Approximation Made Simple, Phys. Rev. Lett. 77 (18) (1996) 3865–3868.
[40] J.P. Perdew, M. Ernzerhof, K. Burke, Rationale for mixing exact exchange with density functional approximations, J. Chem. Phys. 105 (22) (1996) 9982–9985.
[41] S. Grimme, J. Antony, S. Ehrlich, H. Krieg, A consistent and accurate ab initio parametrization of density functional dispersion correction (DFT-D) for the 94 elements H-Pu, J. Chem. Phys. 132 (15) (2010) 154104, https://doi.org/10.1063/1.3382344.
[42] G. Kresse, J. Hafner, Ab initio molecular dynamics for liquid metals, Phys. Rev. B 47 (1993) 558.
[43] C. Su, H. Jiang, J. Feng, Two-dimensional carbon allotrope with strong electronic anisotropy, Phys. Rev. B 87 (2013), 075453.
[44] K. Mathew, R. Sundararaman, K.L. Weaver, T.A. Arias, R.G. Hennig, Implicit solvation model for density-functional study of nanocrystal surfaces and reaction pathways, J. Chem. Phys. 140 (2014) 084106–084114.
[45] D. Sheppard, R. Terrell, G. Henkelman, Optimization methods for finding minimum energy paths, J. Chem. Phys. 128 (2008), 134106.
[46] S. Maintz, V.L. Deringer, A.L. Tchougreeff, L. Andrei, R. Dronskowski, A tool to extract chemical bonding from plane-wave based DFT, J. Comput. Chem. 37 (2016) 1030–1035.
[47] E.F. Holby, G. Wang, P, Zelenay, Acid Stability and Demetalation of PGM-Free ORR Electrocatalyst Structures from Density Functional Theory: A Model for "Single-Atom Catalyst" Dissolution, ACS Catal. 10 (2020) 14527–14539.
[48] X. Guo, S. Lin, J. Gu, S. Zhang, Z. Chen, S. Huang, Simultaneously Achieving High Activity and Selectivity toward Two-Electron O_2 Electroreduction: The Power of Single-Atom Catalysts, ACS Catal. 9 (2019) 11042–11054.
[49] CRC Handbook of Chemistry and Physics: A Ready-Reference Book of Chemical and Physical Data, 2011.
[50] J.K. Nørskov, J. Rossmeisl, A. Logadottir, L. Lindqvist, J.R. Kitchin, T. Bligaard, H. Jónsson, Origin of the Overpotential for Oxygen Reduction at a Fuel-Cell Cathode, J. Phys. Chem. B 108 (46) (2004) 17886–17892.
[51] Q. Deng, J. Zhao, T. Wu, G. Chen, H.A. Hansen, T. Vegge, 2D transition metal–TCNQ sheets as bifunctional single-atom catalysts for oxygen reduction and evolution reaction (ORR/OER), J. Catal. 370 (2019) 378–384.
[52] F. Calle-Vallejo, José.I. Martínez, J. Rossmeisl, Density functional studies of functionalized graphitic materials with late transition metals for oxygen reduction reactions, Phys. Chem. Chem. Phys. 13 (34) (2011) 15639, https://doi.org/10.1039/c1cp21228a.
[53] C.W. Xiao, R.J. Sa, Z.T. Cui, S.S. Gao, W. Du, X.Q. Sun, X.T. Zhao, Q.H. Li, Z.J. Ma, Enhancing the hydrogen evolution reaction by non-precious transition metal (Non-metal) atom doping in defective $MoSi_2N_4$ monolayer, Appl. Surf. Sci. 563 (2021), 150388.
[54] A.A. El-Barbary, R.H. Telling, C.P. Ewels, M.I. Heggie, P.R. Briddon, Structure and energetics of the vacancy in graphite, Phys. Rev. B 68 (2003), 144107.
[55] Z. Xue, X. Zhang, J. Qin, R. Liu, TMN_4 complex embedded graphene as bifunctional electrocatalysts for high efficiency OER/ORR, J. Energy Chem. 55 (2021) 437–443.
[56] S. Lu, Z.W. Chen, C. Li, H.H. Li, Y.F. Zhao, Y.Y. Gong, L.Y. Niu, X.J. Liu, T. Wang, C. Q. Sun, Adjustable electronic performances and redox ability of a g-C_3N_4 monolayer by adsorbing nonmetal solute ions: a first principles study, J. Mater. Chem. A 4 (38) (2016) 14827–14838.
[57] S. Lu, C. Li, Y.F. Zhao, Y.Y. Gong, L.Y. Niu, X.J. Liu, T. Wang, Tunable magnetism of 3d transition metal doped $BiFeO_3$, J. Magn. Magn. Mater. 439 (2017) 57–66.

[58] I.C. Man, H. Su, F. Calle-Vallejo, H.A. Hansen, José.I. Martínez, N.G. Inoglu, J. Kitchin, T.F. Jaramillo, J.K. Nørskov, J. Rossmeisl, Universality in Oxygen Evolution Electrocatalysis on Oxide Surfaces, ChemCatChem 3 (7) (2011) 1159–1165.

[59] J.K. Nørskov, T. Bligaard, A. Logadottir, J.R. Kitchin, J.G. Chen, S. Pandelov, U. Stimming, Trends in the Exchange Current for Hydrogen Evolution, J. Electrochem. Soc. 152 (3) (2005) J23, https://doi.org/10.1149/1.1856988.

[60] Y. Zhou, G. Gao, W. Chu, L.-W. Wang, Transition-metal single atoms embedded into defective BC_3 as efficient electrocatalysts for oxygen evolution and reduction reactions, Nanoscale 13 (2) (2021) 1331–1339.